ADVANCED FUNCTIONAL MATERIALS
www.afm-journal.de

Lasing in Crystals Based on 7-Azaindole-Phenylhydrazone Organoboron Compounds

Javier Álvarez-Conde, M. Paz Fernández-Liencres, Sonia B. Jiménez-Pulido, Cristina Martín, Amparo Navarro, Juan Cabanillas-González,* and Eva M. García-Frutos**

The development of efficient organic solid-state lasers requires an in-depth understanding between chemical structure, intermolecular interactions in the crystal phase, and optical and electronic properties. This study highlights these closed dependencies in novel 7-azaindole phenylhydrazone derivatives and their corresponding boron complexes, by deploying a combined approach of experimental techniques and theoretical calculations (Density Functional Theory and Time-Dependent Density Functional Theory) in the solvated and solid-state phase. Notably, it is found that when these compounds, which are weakly emissive in solution, are processed into crystalline microfibers, they experience a sharp emission enhancement and exhibit laser action at low pump fluence thresholds. This is achieved by partially inhibiting structural relaxation, which drives non-radiative decay, a critical factor for effective lasing, highlighting the potential of these materials for future optoelectronic applications.

1. Introduction

At a time when semiconductor technology is indispensable to our daily lives, organic semiconductors have gained popularity mainly due to their light weight, low production cost, low-temperature processing, and mechanical flexibility.[1,2] As a result of these properties, organic semiconductors have been key in various applications, including sensors,[3] organic solar cells,[4] organic light emitting diodes (OLEDs),[5] and organic solid-state lasers (OSSLs).[6–9]

Organic optoelectronics is widely recognized as a solution-based processing technology and although the primary building block is a molecular entity, the device performance is largely determined by molecular packing. This packing is driven by intermolecular interactions, such as dispersion forces, electrostatic interactions, and hydrogen bonding, which play a crucial role in defining their macroscopic properties.[10–12] An important pitfall for solid state light emission is aggregation-caused quenching (ACQ),[13] where the strong coupling between the electronic and vibrational degrees of freedom of the organic moieties quenches the emission despite strong luminescence in the parent molecule in solution. Significant progress has been made in improving emission in the solid state by reducing the non-radiative pathways in favor of

J. Álvarez-Conde, E. M. García-Frutos
Instituto de Ciencia de Materiales de Madrid (ICMM)
CSIC
Ciudad Universitaria de Cantoblanco
Madrid 28049, Spain
E-mail: emgfrutos@icmm.csic.es

J. Álvarez-Conde, J. Cabanillas-González
Madrid Institute for Advanced Studies
IMDEA Nanociencia
Calle Faraday 9
Ciudad Universitaria de Cantoblanco
Madrid 28049, Spain
E-mail: juan.cabanillas@imdea.org

M. P. Fernández-Liencres, A. Navarro
Departamento de Química Física y Analítica
Facultad de Ciencias Experimentales
Universidad de Jaén
Campus Las Lagunillas, Jaén 23071, Spain
E-mail: anavarro@ujaen.es

S. B. Jiménez-Pulido
Departamento de Química Inorgánica y Orgánica
Facultad de Ciencias Experimentales
Universidad de Jaén
Campus Las Lagunillas, Jaén 23071, Spain

C. Martín
Departamento de Química Física
Facultad de Farmacia
Universidad de Castilla-la Mancha
Avda. Dr. José María Sánchez Ibáñez, s/n, Albacete 02071, Spain

E. M. García-Frutos
Departamento de Química Orgánica y Química Inorgánica
Universidad de Alcalá
Alcalá de Henares, Madrid 28805, Spain

The ORCID identification number(s) for the author(s) of this article can be found under https://doi.org/10.1002/adfm.202402859

DOI: 10.1002/adfm.202402859

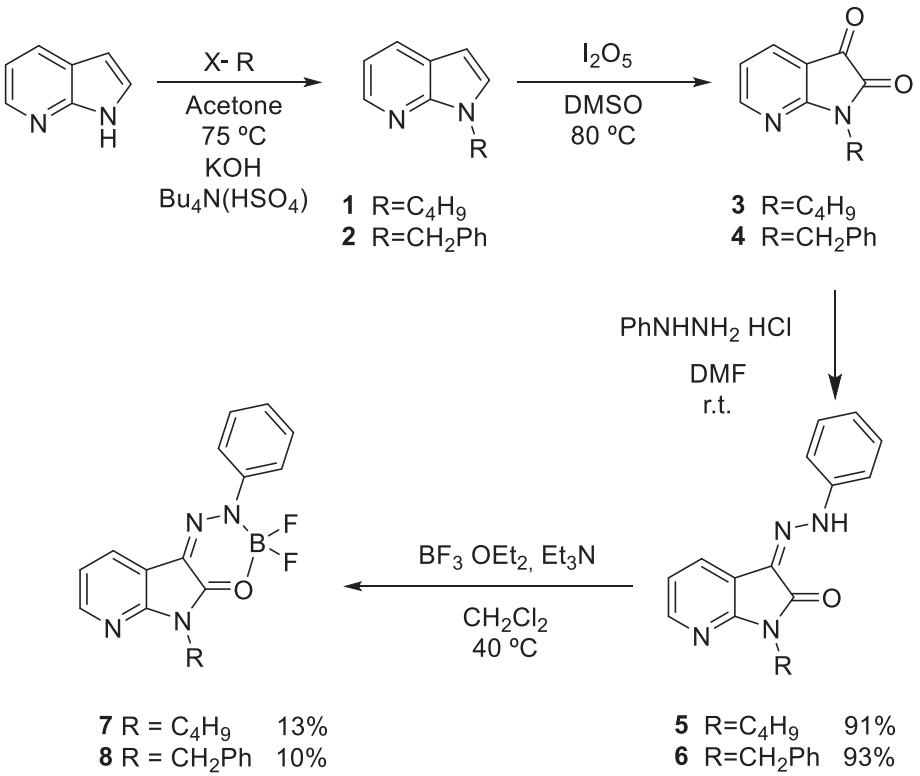

Scheme 1. Synthetic route to obtain 7-azaindole-hydrazone organoboron complexes **7** and **8**.

the radiative ones, leading to a new generation of fluorogens with aggregation-induced emission (AIEgens).[14,15]

Up to this point, all endeavors for the conversion of ACQ systems into AIEgens could be categorized into two principal strategies: (a) chemical modification of the chromophore and (b) aggregation control.[16–18] The modification of chromophores, as exemplified by side-chain engineering, and the facilitation of radiative pathways by restriction of intramolecular vibrations (RIV) have been widely discussed in the scientific literature.[19–21] Nevertheless, although research into the manipulation of chromophores during aggregation or subsequent processes has recently increased, it is still limited, hindering the full development and optimization of AIEgens.

The insufficient research about the aggregation process cannot be limited to the physical properties of these materials compared to their amorphous counterparts due to a reduction in the disorder arrangement. There is also a lack of understanding regarding the molecular platform and processes required to facilitate the necessary molecular interactions for achieving long-range homogeneity and highly ordered molecular packing, which are essential for optimal carrier mobility and quantum efficiency in the solid state.[22–24] Unravelling this information will also facilitate the assembly of organic platforms into different crystal geometries, allowing anisotropic behavior along different axes.[21] This is crucial for optical applications such as optical waveguides or lasers.[25]

Herein, a previously known core in AIEgens, 1H-pyrrolo(2,3-b)pyridine (7-azaindole),[26–29] has been used to elucidate how optoelectronic properties can be tuned simultaneously by chemical modification and manipulation during or after aggregation. Specifically, side-chain engineering combined with boron complexation in the hydrazone were the approaches used to enhance the chemical platform, while molecular precipitation was employed to induce the crystalline structure. The combined experimental and theoretical approach (DFT and TD-DFT) probes that the incorporation of boron complex controls the isomerization of the double bond through *E*-to-*Z* or *trans*-to-*cis* transformation in the final complexes. Furthermore, the control of the solvent precipitation through the antisolvent method allows to form needles with notable luminescence and random lasing properties.

2. Results and Discussion

2.1. Synthesis

The synthesis of 7-azaindole-phenylhydrazone organoboron complexes (**7** and **8**) was achieved by a coordination of BF_2 to previous hydrazone derivatives (**Scheme 1**, see Supporting Information). To prepare 7-azaindole-hydrazone derivatives (**5** and **6**), commercially available 7-azaindole was first *N*-alkylated to increase the solubility of the scaffold under regular conditions using 1-iodobutane or benzyl bromide in the presence of KOH and $Bu_4N(HSO_4)$ in acetone affording **1** and **2**. Then, an oxidation by I_2O_5 in DMSO was achieved to obtain the azaisatines **3** and **4**. The synthesis of hydrazone derivatives was performed by a condensation reaction of azaisatines **3** and **4** with phenylhydrazine hydrochloride in DMF at room temperature affording hydrazone derivatives **5** and **6** with a 91% and 93% of yield, respectively.

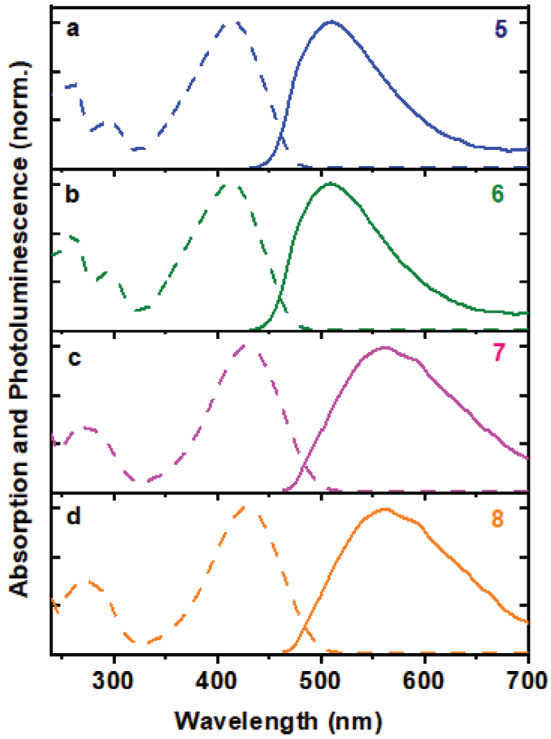

Figure 1. Normalized absorption and PL spectra of a) **5**, b) **6**, c) **7**, and d) **8** in THF. Solution concentrations were 10 μM in all cases.

Finally, the BF_2 coordination was accomplished by treatment with ($BF_3.OEt_2$) and Et_3N as the base in CH_2Cl_2 leading to the desired **7** and **8** compounds yielding 13% and 10%.

2.2. Molecular Structure and Photophysical Properties in Solution

The absorption and photoluminescence (PL) spectra of the four compounds (**Figure 1** and **Table 1**) in THF do not exhibit vibronic progressions, being the maxima of the dominant bands located in the 415–430 and 510–562 nm spectral range respectively. Note that BF_2 coordination in **7–8** manifests in a clear absorption and PL bathochromic shift (13 nm / 98 meV and 53 nm / 225 meV) respect to **5–6**, which can be understood as due to an enhanced planarity forced by boron coordination. Similar effects were reported by Zheng et al.[30] in isatin-phenylhydrazones upon BF_2 coordination. It is worth noting that even in this case, the photoluminescence quantum efficiency (Φ) for the four compounds is rather low (<1%) indicating a dominant non-radiative decay pathway, as it was previously observed for other BODIHY series where the lowest S_1 is a dark state.[29]

Table 1. Absorbance (λ_{abs}), PL excitation (λ_{exc}) and PL emission (λ_{emis}) peak wavelengths (in nm) and Stokes shift (in cm^{-1}) of compounds **5–8** in THF solution.

Compound	λ_{abs}	λ_{exc} (nm)	λ_{emis}	Stokes shift
5	260/295/415	415	510	4488
6	260/295/414	415	510	4547
7	274/428	428	562	5570
8	274/428	428	562	5570

DFT and TD-DFT calculations were carried out considering THF solvation implicitly in order to assign the absorption and photoluminescence bands to specific electronic transitions. **Table 2** lists the vertical electronic transitions calculated for these compounds. TD-DFT calculations are in good agreement with the experimental maximum absorption wavelengths with deviations <0.2 eV for PBE0, and ≈0.4 eV for M06-2X and CAM-B3LYP. According to the theoretical calculations, the main band observed ≈415 nm (428 nm) in **5(6)** and **7(8)**, was assigned to the lowest $S_0 \rightarrow S_1$ transition with high oscillator strength values (f ≈0.7–0.8), showing a high HOMO→LUMO contribution (≥97%) and charge transfer character. The frontier molecular orbitals are represented in Figure S1 (Supporting Information). In general, the HOMO is delocalized throughout the molecule, regardless of the R substituent at the N1 position, whereas the LUMO is less extended toward the phenyl attached to the hydrazone. Therefore, the electronic transition is nearly independent of the N1 substituent, which explains why the alkyl versus phenyl substitution did not translate into significant spectral changes in solution.

Figures S2–S6 (Supporting Information) show some selected dihedral angles of the optimized molecular geometry in THF solution for the ground and first excited state. Table S1 (Supporting Information) lists their relative energies considering Z and E isomers in the case of compounds **5** and **6**. Z configuration is predicted to be more stable than E isomer in the ground state with energy differences ≈5 kcal mol^{-1}, resulting in planar structures in both Z and E isomers regardless of the functional used. The higher stabilization of the Z isomer for compounds **5** and **6** in the ground state could be favored by the intramolecular hydrogen bonding between the carbonyl and the hydrazone group with O···H-N distance in the 1.9-2.0 Å range, in agreement with the experimental X-ray crystal structure. It should be noted that **7** and **8** can only be obtained from the Z configuration although the E isomer could be present in solution during the coordination reaction of BF_2 in **7–8** at 40 °C. Compounds **7** and **8** show non-planar geometries in the ground state with dihedral angles between the phenyl ring and the azaindole-hydrazone-organoboron platform in the 26°–29° range. These compounds become completely planar in solid-state, as confirmed from the X-ray crystal structure.

Table 3 shows the calculated emission using state-specific solvation approach (SS) along with the maximum PL emission wavelengths for comparison. Once again, the functional PBE0 reproduces more accurately the experimental data with energy differences ≈0.2 eV, and ≈0.4 eV for M06-2X and CAM-B3LYP. As shown in Table 3, PBE0 predicts different values for the $S_1 \rightarrow S_0$ transition in compounds **5** and **6**, (501 and 486 nm, respectively), when the SS approach is employed, despite both compounds displaying PL with maxima at 510 nm. In turn, the linear response approach (LR) was used with PBE0 resulting in similar values for the $S_1 \rightarrow S_0$ transition, 511 and 512 nm for **5** and **6**, respectively. Figures S2–S6 (Supporting Information) show the optimized molecular geometries in the first excited state S_1. Compounds **5** and **6** (Z isomer) in S_1 remain planar as in the S_0 ground state using PBE0 and CAM-B3LYP. However, M06-2X twists the hydrazone group ≈90° from S_0 to S_1. Compounds **7** and **8** planarize in the first excited state with almost zero dihedral angle between the phenyl ring and the azaindole-hydrazone-organoboron platform

Table 2. Experimental absorption (λ_{ab}^{exp}) and calculated vertical electronic transitions ($\lambda_{vert\text{-}ab}^{calc}$) (in nm and eV in parenthesis), oscillator strength (f), and main components of the electronic transitions (% contribution) at the TD-M06-2X/6-31+G**, TD-PBE0/6-31+G**, and TD-CAM-B3LYP/6-31+G** levels of theory in THF solution. λ_{ab}^{exp} corresponds to the wavelength of the absorption maximum.

Comp.	λ_{ab}^{exp}	$\lambda_{vert\text{-}ab}^{calc}$	Transition	f	% Contribution
M06-2X/6-31+G**					
5	415 (2.99)	367 (3.38)	$S_0 \rightarrow S_1$	0.82	H → L (98)
		299 (4.14)	$S_0 \rightarrow S_3$	0.11	H-1 → L (90)
		256 (4.85)	$S_0 \rightarrow S_4$	0.15	H → L+1 (57), H-1 → L+1 (19)
6	414 (2.99)	368 (3.37)	$S_0 \rightarrow S_1$	0.84	H → L (98)
		298 (4.16)	$S_0 \rightarrow S_3$	0.10	H-1 → L (90)
		256 (4.85)	$S_0 \rightarrow S_4$	0.13	H → L+1 (55), H-1 → L+1 (17)
7	428 (2.90)	377 (3.29)	$S_0 \rightarrow S_1$	0.79	H → L (98)
		289 (4.29)	$S_0 \rightarrow S_3$	0.10	H-1 → L (88)
		254 (4.89)	$S_0 \rightarrow S_5$	0.21	H → L+1 (65), H-1 → L+1 (17)
8	428 (2.90)	377 (3.29)	$S_0 \rightarrow S_1$	0.79	H → L (97)
		288 (4.31)	$S_0 \rightarrow S_3$	0.06	H-1 → L (73)
		254 (4.89)	$S_0 \rightarrow S_5$	0.21	H → L+1 (65), H-1 → L+1 (13)
PBE0/6-31+G**					
5	415 (2.99)	398 (3.11)	$S_0 \rightarrow S_1$	0.71	H → L (98)
		341 (3.63)	$S_0 \rightarrow S_2$	0.21	H-1 → L (96)
6	414 (2.99)	399 (3.11)	$S_0 \rightarrow S_1$	0.74	H → L (98)
		340 (3.65)	$S_0 \rightarrow S_2$	0.19	H → L+1 (96)
7	428 (2.90)	400 (3.10)	$S_0 \rightarrow S_1$	0.71	H → L (100)
		338 (3.67)	$S_0 \rightarrow S_2$	0.10	H-1 → L (97)
8	428 (2.90)	400 (3.10)	$S_0 \rightarrow S_1$	0.71	H → L (100)
		338 (3.67)	$S_0 \rightarrow S_2$	0.10	H-1 → L (92)
CAM-B3LYP/6-31+G**					
5	415 (2.99)	367 (3.38)	$S_0 \rightarrow S_1$	0.82	H → L (97)
		301 (4.12)	$S_0 \rightarrow S_2$	0.10	H-1 → L (77), H-3 → L (16)
		256 (4.84)	$S_0 \rightarrow S_4$	0.17	H → L+1 (54), H-1 → L+1 (25)
6	414 (2.99)	368 (3.37)	$S_0 \rightarrow S_1$	0.84	H → L (97)
		299 (4.15)	$S_0 \rightarrow S_2$	0.10	H-1 → L (59), H-4 → L (28)
		256 (4.85)	$S_0 \rightarrow S_4$	0.14	H → L+1 (52), H-1 → L+1 (21)
7	428 (2.90)	374 (3.32)	$S_0 \rightarrow S_1$	0.76	H → L (98)
		295 (4.21)	$S_0 \rightarrow S_2$	0.03	H-1 → L (68), H-5 → L (23)
		253 (4.89)	$S_0 \rightarrow S_5$	0.19	H → L+1 (53), H-1 → L+1 (23), H-1 → L (14)
8	428 (2.90)	374 (3.32)	$S_0 \rightarrow S_1$	0.77	H → L (98)
		294 (4.22)	$S_0 \rightarrow S_2$	0.02	H-1 → L (53), H-7 → L (34)
		254 (4.89)	$S_0 \rightarrow S_5$	0.19	H → L+1 (53), H-1 → L+1 (17)

regardless the functional used (see Figures S4 and S5, Supporting Information). This result could justify the larger Stokes shift observed in **7** and **8** compared to **6** and **7**, which do not undergo strong geometric relaxation in the excited state.

The calculated Huang-Rhys factors (HR) are shown in Table S2 (Supporting Information) and **Figure 2**. Figure 2 depicts the HR values for a wide range of different modes for compounds **5** and **6**, exhibiting in all cases low HR factors (≤0.7) characteristic of moderate electron-phonon coupling. Compounds **7** and **8** denote instead the appearance of low frequency vibrational modes with large HR values (HR = 6 at 20 and 25 cm^{-1} in **7** and HR ≈8 at 18 cm^{-1} in compound **8**). According to the atomic displacements associated with those vibrational modes represented in Figure 2 for compounds **7** and **8**, these are wagging vibrations that involve the phenyl in the hydrazone moiety and the C_4H_9 and CH_2Ph lateral substituents and could somehow preponderate. This result is in concordance with the geometry changes described above when going from S_0 to S_1.

The low emission quantum yields of **5**, **6**, **7**, and **8** could be ascribed to different mechanisms. In **7** and **8**, luminescence quenching could be attributed to excited state de-activation due to strong coupling with wagging vibrations, whereas photoisomerization could be the more likely reason for the low emission nature of **5** and **6**, in view of the low HR factors of the active vibrational modes predicted in these compounds. Indeed, reversible Z↔E hydrazone isomerization has been widely reported and

Table 3. Maximum fluorescence emission wavelengths (λ_{em}^{max}), quantum yield (Φ) and calculated emission wavelengths ($\lambda_{vert\text{-}em}^{calc}$) (in nm and eV in parenthesis) for the $S_1 \rightarrow S_0$ transition in THF solution calculated at the TD-M06-2X/6-31+G**, TD-PBE0/6-31+G**, and TD-CAM-B3LYP/6-31+G** levels of theory.

Comp.	λ_{em}^{max}	Φ(%)	$\lambda_{vert\text{-}em}^{calc}$	f	% Contr.
M06-2X/6-31+G**					
5	510 (2.43)	<0.0	1459 (0.85)	0.00	H → L (90)
6	510 (2.43)	<0.01	1505 (0.82)	0.00	H → L (90)
7	562 (2.21)	<0.01	475 (2.61)	0.79	H → L (99)
8	562 (2.21)	<0.01	478 (2.60)	0.80	H → L (99)
PBE0/6-31+G**					
5	510 (2.43)	<0.01	501 (2.48) // 482 (2.57)	0.70	H → L (99)
6	510 (2.43)	<0.01	486 (2.55) // 480 (2.58)	0.75	H → L (100)
7	562 (2.21)	<0.01	506 (2.45) // 511 (2.43)	0.73	H → L (100)
8	562 (2.21)	<0.01	508 (2.44) // 512 (2.42)	0.74	H → L (100)
CAM-B3LYP/6-31+G**					
5	510 (2.43)	<0.01	443 (2.80)	0.83	H → L (98)
6	510 (2.43)	<0.01	448 (2.79)	0.85	H → L (98)
7	562 (2.21)	<0.01	483 (2.57)	0.77	H → L (98)
8	562 (2.21)	<0.01	485 (2.56)	0.77	H → L (98)

*Z isomer in compounds **5** and **6**. SS // LR approach in PBE0.

exploited in many applications such as molecular switches, sensors, and photoreactive materials with appreciable changes in photoisomerization quantum yield.[31–34] Table S1 (Supporting Information) includes the relative energies of the optimized first excited state for compounds **5** and **6** (both Z and E isomers) and compounds **7** and **8**. Unlike the ground state in which the Z isomer is more stable than E isomer for compounds **5** and **6**, in the first excited state the E isomer becomes more stable with energy differences ≈9 kcal mol^{-1} using PBE0 and ≈6 kcal mol^{-1} using CAM-B3LYP with respect to the Z isomer (except in compound **6** using M06-2X for which the Z isomer is more stable in S_1).

These mechanisms could be altered in solid-state, since photoisomerization and vibrational relaxation could be sterically hindered. The characterization of the single crystal structures and their effect on the optical properties are discussed next.

2.3. Single-Crystal X-Ray Structures of 5–8

Single-crystal X-ray diffraction experiments were conducted with the aim of understanding the nature of intra- and inter-molecular interactions present in the ligands **5** and **6** and the boron compounds **7** and **8**. Compounds **5**, **7**, and **8** crystallized in monoclinic $P2_{1/c}$ and compound **6** in triclinic $P\bar{1}$ symmetry with two crystallographically independent molecules in the asymmetric unit. Crystallographic data for these compounds and the most significant bond distances and angles are listed in Table S3 and Figures S7–S10 (Supporting Information).

The crystal structure shown in **Figure 3** reveals a nearly planar molecular conformation with between 9.97° (**5**), 7.81° (**6**), 8.98° (**7**), and 2.17° (**8**) azaindole-phenyl dihedral angles. On the other hand, the alkyl chain (phenyl) substituent in N1 show dihedral angles with respect to the azaindole platform of 88.5° (77.9°) in **5** (**7**) and 74.9° (87.9°) in **6** (**8**). The ligands **5** and **6** present an intramolecular hydrogen bond between the ketone and N–H group. The O···H–N distance shows a value of 2.787 Å in compound **5** and 2.805 and 2.778 Å in compound **6** for the two molecules in the asymmetric unit, respectively.

The boron atom adopts a slightly distorted tetrahedral geometry (N4, O1, F1, F2) in the **7** and **8**, with bond angles ranging from 105 to 111°, deviating from the ideal value of 109.5°. In addition, it is displaced with respect to the O1-C1-C2-N3-N4-B1 plane in 0.108(3)° and 0.081(3)° in **7** and **8**, respectively. On the other hand, the formation of *N,O*-chelate six-membered rings contributes to the construction of the rigid three-ring-fused π-conjugated skeletons in compounds **7** and **8**.

The C1 = O1 bond length in **5** and **6** (1.227 Å) is similar to typical C = O bond lengths (ca. 1.20 Å). However, this distance is longer in **7** and **8** (1.28 Å) which is attributed to the influence of the O-B coordination bond. The O1–B1 and N4–B1 bond distances are similar in both complexes, 1.50 Å (**7**) and 1.58 Å (**8**), respectively, and close to those of other related four-coordinate boron compounds.[35] The C–N (1.32 Å), N–N (1.31 Å), and C–C (1.42 Å) bond lengths within the boron heterocycle are between those expected for single and double bonds of the respective atoms, indicating that the π-electron systems are highly delocalized.

The supramolecular structures in all compounds are formed by π–π interactions and intermolecular interactions classified as C–H···X (X = F, N, O, Cg) and C–H···H–C hydrogen bond. Table S4 (Supporting Information) shows the geometrical parameters associated with these π-π interactions. In complex **7**, the presence of the bora-cycle favors π–π interactions compared to compound **5**, since interplanar interactions decrease, increasing the π-π overlap. Compound **5** assembles in a slip-stacked arrangement with inter-plane distances ≈3.4 Å (Figure S7b, Supporting Information). These columns are interconnected by two hydrogen bonds C–H···N and C–H···O, with distances of 2.732 and 2.587 Å, respectively (see Figure S7, Supporting Information),

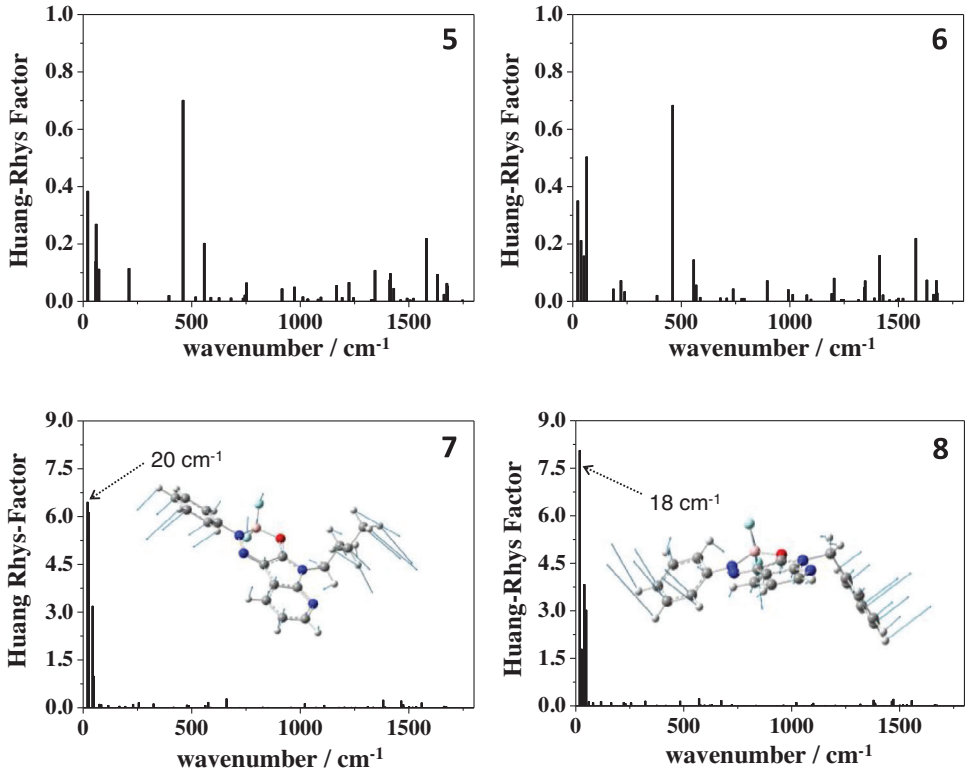

Figure 2. Huang-Rhys factors versus normal mode wavenumbers (in cm^{-1}) calculated for compounds **5**, **6**, **7**, and **8** in THF at the TD-PBE0/6-31+G** level of theory. The atomic displacements of some selected vibrational modes were included for compounds **7** and **8**.

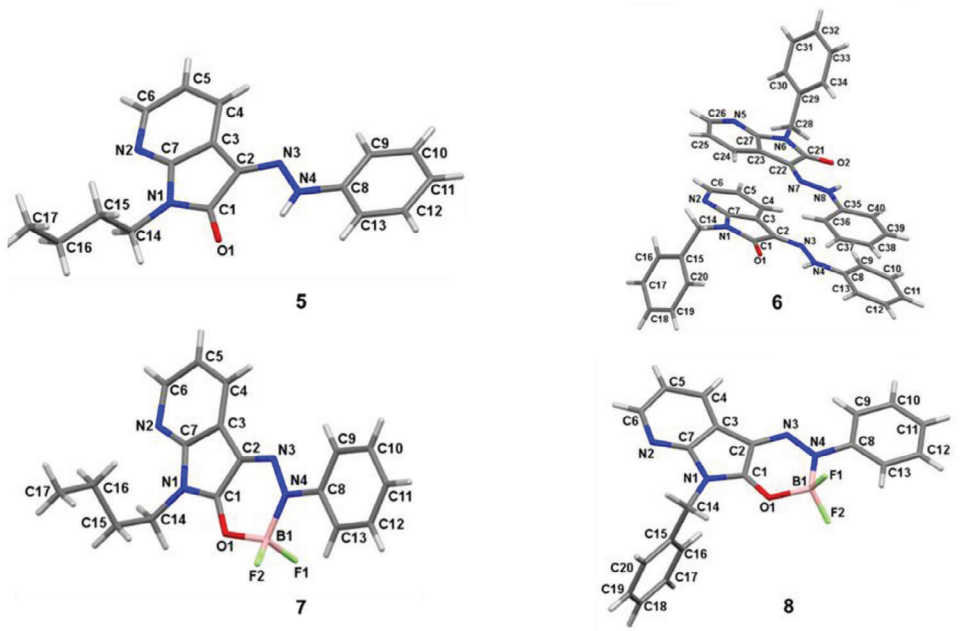

Figure 3. Asymmetric units and numbering scheme of compounds **5**–**8**.

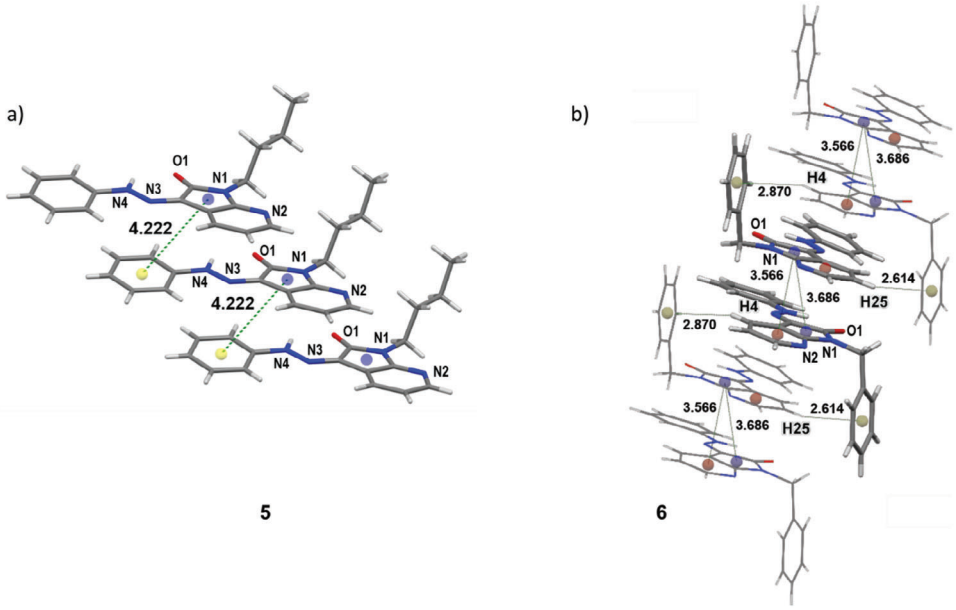

Figure 4. Crystal packing in compounds a) **5** and b) **6**.

endowing the crystal with a 3D nearly sandwich herringbone with weak π-π interactions between the pyrrol and phenyl rings and distances ≈4.222 Å (see **Figure 4**).

As shown in Figure 4, **6** molecules are instead cofacially stacked through head-to-head π–π stacking interactions with the phenyl group substituted in N1 atom in *trans* position to minimize steric interactions. The 3D network is stablished by two hydrogen bonds C—H···N (2.720 Å) and very weak C—H···H—C and C—H···Cg interactions (2.614 Å) (Figure S8, Supporting Information).

In the molecular packing of **7** and **8**, a weak overlapping through head-to-head π–π stacking interactions was observed in both complexes (Table S4, Supporting Information) in which the six membered ring was formed by the presence of the boron atom. For complex **7**, the molecules stack through π–π interactions and B-F2···CgA bonds (see **Figure 5**). The 3D structure is formed through C12-H12···CgB interactions in which the angle of the C12-H12 bond with the π-plane is 82° so that the adjacent molecules are quasi perpendicular (Figure S9, Supporting Information).

In compound **8**, the supramolecular structure is dominated by two weak contacts between the phenyls rings in N4 substitution of neighboring molecules (C—H···H—C, distance 2.320 Å), and C—H···F bonds (d = 3.325(3) Å and <(F2···H5-C5) = 148°). The π–π interactions in **8** are weaker than in the other studied compounds with distances ≈3.8 Å (see Figure 5), which may be due to

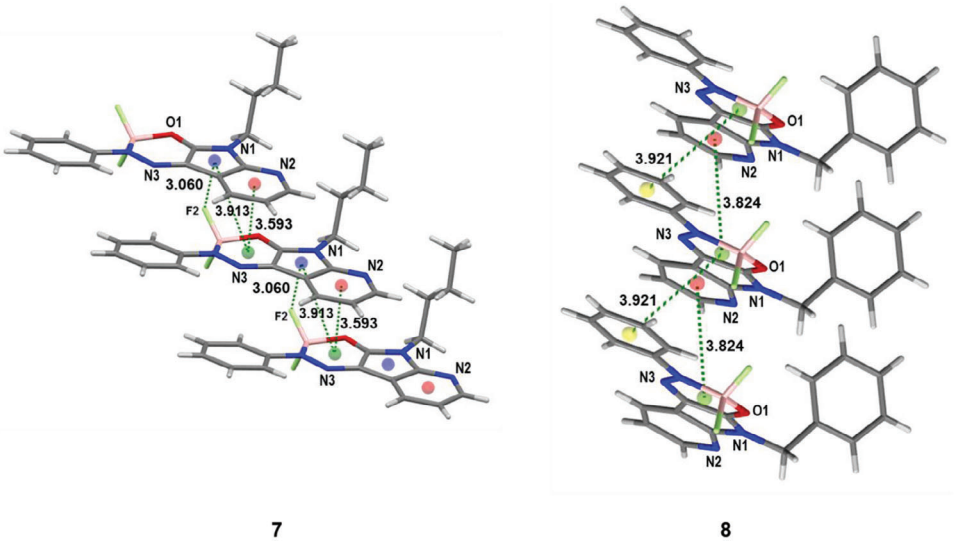

Figure 5. Crystal packing in compounds **7** and **8**.

Table 4. Experimental emission (λ_{em}^{exp}), quantum yield (**Φ**), and calculated $S_1 \rightarrow S_0$ transition ($\lambda_{vert\text{-}em}^{calc}$) (in nm and eV in parenthesis) in solid state calculated at the ONIOM (TD-PBE0/6-31+G**/UFF) level of theory.

			One active molecule			Two active molecules		
Comp.	λ_{em}^{exp}	Φ(%)	$\lambda_{vert\text{-}em}^{calc}$	f	% Contr.	λ_{emis}^{calc}	f	% Contr.
5	515 (2.41)	21	532(2.33)	0.085	H → L (89)			
6	519 (2.39)	7	535(2.32)	0.090	H → L (89)			
7	550 (2.25)	19	495(2.51)	0.486	H → L (100)	662(1.88)	0.004	H → L (99)
8	582 (2.13)	19	484(2.56)	0.541	H → L (100)	672(1.85)	0.001	H → L (99)

the perpendicular arrangement of the phenyl group in N1 which shifts the molecular planes increasing the interaction between adjacent molecules (Figure S10, Supporting Information).

2.4. Photophysical Properties in Solid State

Figure S11 (Supporting Information) shows UV–vis and PL spectra of the four compounds measured in solid-state. The PL peak wavelengths are collected in **Table 4** along with the quantum yields (**Φ**). Compared to solution, we observe enhanced luminescence in solid-state with quantum yields of 21%, 7%, 19%, and 19% for compounds **5**, **6**, **7**, and **8**, respectively. The time-correlated single photon counting revealed that the average lifetimes are enlarged from 1.51 and 0.65 ns for compounds **5** and **6** respectively to 1.67 and 1.85 ns for **7** and **8**, respectively. This behavior can be explained in terms of structural rigidity and when the boron cycle is presented.

In order to gain further insight into the photophysical properties in the solid state, theoretical calculations were performed using the time-dependent density functional theory (TD-DFT) method on the crystal structures. ONIOM methodology was used defining a cluster with enough molecules extracted from the experimental X-ray crystal to mimic the crystalline environment as described in Computational Details Section. **Figure 6** shows the ONIOM clusters built for each compound. Initially, the molecular geometry of a central active molecule in the ground and first excited state was optimized (high level with DFT) while the crystallographic positions of the surrounding molecules were kept frozen (low level with UFF). The model clusters are represented in Figure 6a–d, for compounds **5**, **6**, **7**, and **8**, respectively. Table 4 lists the calculated emission from the first excited state S_1 obtaining a good concordance between experimental and theoretical results with energy differences <0.3 eV. As already observed in the calculations in solution, the greater differences between experimental and theoretical data are obtained for compounds **7** and **8**. Although discrepancies are within the typical deviation range in this type of photophysical studies, it is striking that the experimentally observed red shift in the solid state emission, (from 515–519 nm in **5–6** to 550–582 nm in **7–8**), is not predicted by the model cluster (from 532–535 nm in **5–6** to 495-484 nm in **7–8**) (see Table 4). Instead, a different approach was followed to account for the electronic couplings ascribed to π-π stacking in **7** and **8** crystals, which involved considering two central active molecules selected and optimized in the ground and first excited state (see Figure 6e,f). As a consequence, to ensure that the two central molecules are totally surrounded by neighboring molecules, the number of neighboring molecules increased from 15 to 21 in **7** and from 12 to 17 in **8**. Table 4 shows the calculated $S_1 \rightarrow S_0$ energy transition according to the *two active molecules* model. As observed, the new model cluster predicts a red shift from 532–535 nm to 667–672 nm for **5–6** and **7–8**, respectively, in agreement with the experimental observations, (see Table 4).

2.5. Photophysical Properties in Microcrystals

Microcrystals from **5**, **6**, **7**, and **8** were obtained as described in the materials and methods section. This protocol afforded clustered needles of ≈100 μm length scale (**Figure 7**a–d). Remarkably, the end facets from these needles display stronger luminescence than in the bulk, confirming that the luminescence in these structures is efficiently waveguided and out-coupled at the needle tips. The μ-PL spectra from individual crystals of each type were obtained and compared with the corresponding PL spectra in solution. The PL spectra of a **5**(**6**) needle is composed of a 0-0 vibronic shoulder at 480 nm, a PL peak at 515(519) nm and a smeared out shoulder at 550 nm (Figure 7). The weaker 0-0 PL transition in the crystal compared to solution is most likely related to self-absorption.[36,37] Indeed, the spectra from **5** and **6** needles differ significantly from the PL spectra in solution, but match with the ones observed in solid state, where the red shift was explained as a result of strong electronic inter-molecular coupling. BF_2 complexation in **7** and **8** is translated into needles exhibiting a PL red-shift of 36 nm (16 meV) and 56 nm (230 meV), with respect to the PL spectra of **5** and **6** needles (Figure 7) respectively, and in the same way align with the solid state spectra.

The PL from a **7** needle depicts a maximum at 550 nm with a shoulder at 582 nm, whereas the PL from an **8** needle is broader being centered at 582 nm. These slight differences could indicate that the different peripheral groups in **7** and **8** lead to changes in the crystal structure. Noteworthy, in contrast to **5** and **6**, the PL spectra of needles in **7**(**8**) resemble the PL in solution, despite spectral broadening and minor dielectric spectral shifts. A possible explanation could be based on the same planar S_1 molecular geometries in **7**(**8**) in solution and solid state, as already described in the previous sections. This scenario is different in **5**(**6**) due to photoisomerization, which gives rise to a different S_1 conformation in solution respect to solid-state, where photoisomerization remains hindered. Notably, the PL spectra of compound **8** show less vibronic structure compared to compound **7**. The reason for this difference is unclear. Considering that changes in vibronic coupling can occur in the solid state, we hypothesize that the wagging vibrations in compound **8** might be partially restricted due

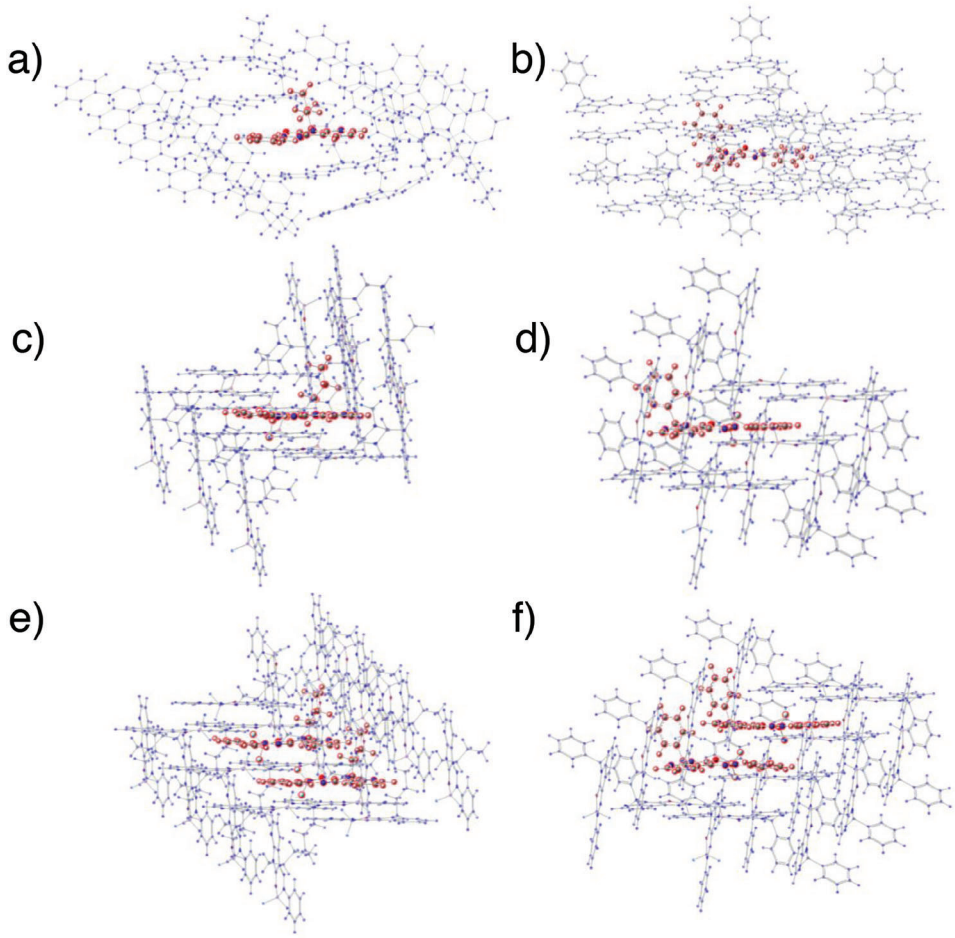

Figure 6. QM/MM model clusters for the studied compounds. The active molecule (in red) is treated as high level (PBE0/6-31+G**) and the surrounding molecules (in blue) as low level (UFF). Clusters **a)**, **b)**, **c)** and **d)** define one central active molecule for **5**, **6**, **7** and **8**, respectively. Clusters **e)** and **f)** define two central active molecules for **7** and **8**, respectively.

to molecular packing and the larger displaced volume associated to the phenyl substitution. This effect could result in the loss of vibronic features in the spectrum.

2.6. Random Lasing in 7 and 8 Needles

Needles based on **7** and **8** displayed in addition stimulated emission in contrast to **5** and **6** where only spontaneous emission was observed. Stimulated emission in **7** and **8** manifested in the form of random lasing when pumped at sufficiently high fluences. Lasing experiments were performed by pumping an ensemble of crystals with 0.3 ns laser pulses of variable energy at 355 nm and detecting the emission spectra as function of pump fluence. Upon gradual rising the pump fluence, narrow linewidth peaks emerge from the characteristic PL spectra, (**Figure** 8a,c). Linewidth narrowing and super-linear fluence dependence of emission in both compounds are illustrated in Figure 8b,d, each panel featuring the dependence of the output intensity and full width at high maximum (FWHM) with pump fluence. When the pump fluence is increased, an abrupt drop in FWHM appeared (Figure 8b,d) accompanied by a sudden change in the slope of the excitation input versus emission output curve, (triangles, Figure 8b,d). According to Figure 8a,c, the dominant lasing modes appear centered at 599 nm in both microneedles, whereas secondary peaks appear upon further rising the pump fluence, being red shifted in **8**. Note that there is not an equal spacing between the lasing modes, ruling out the possibility of them being ascribed to Fabry-Perot oscillations, and more in line with a random lasing origin. The random cavity could be supported by the presence of scattering centers at the crystals or boundaries between many crystals. Since random lasing emerged from clustered instead of isolated microneedles, we conjecture that the random cavity could be the result of multiple reflections from randomly distributed scattering centers within the clusters, leading eventually to closed loops.[38–40]

The obtained random lasing thresholds are comparable to others found in the literature. Varghese et al. reported random lasing in platelets and wires based on distyrylbenzene derivatives[41,42] with 2.4 and 4.8 mJ cm^{-2} fluence thresholds. Yoon et al. reported random lasing with 2.1 mJ cm^{-2} threshhold in α-MODCS(needle) distyrylbenzenes.[43] Lasing thresholds of 0.5 mJ cm^{-2} or lower were instead reported

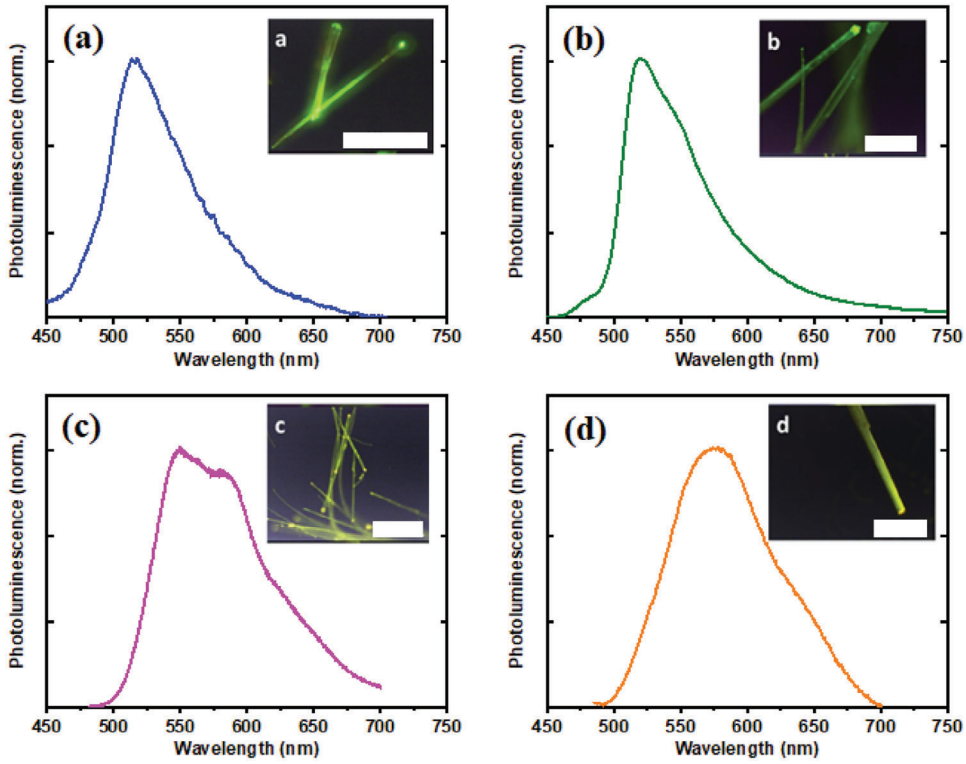

Figure 7. a–d) Normalized photoluminescence of single **5–8** needles. The photoexcitation wavelength was 365 nm. Fluorescence microscopy images are shown in the insets with a 100 µm length scale bar.

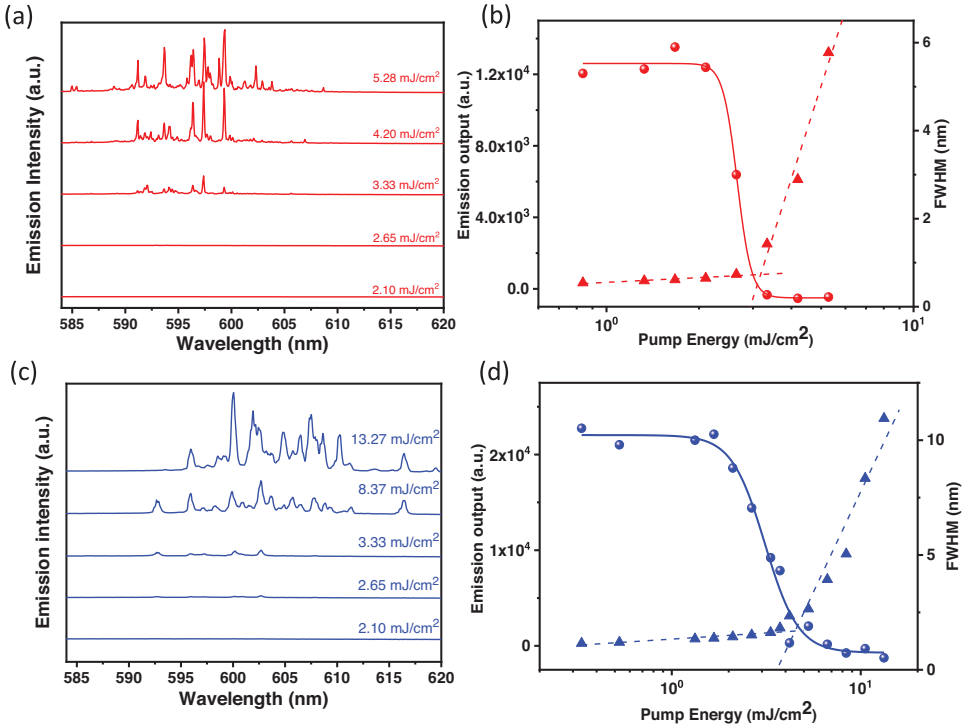

Figure 8. a,c) Random lasing from **7** and **8** needles. b,d) Emission output (triangles, dotted lines) and full width at half maximum (circles, solid line) as a function of pump fluence for **7** and **8**, respectively, upon 355 nm photoexcitation.

in 1,1,4,4-tetraphenyl-1,3-butadiene platelets,[44] in 2,7-diphenyl-9H-fluorene needles,[45] or in para-sexyphenyl nanofibers.[46]

3. Conclusion

This study reports on the synthesis and characterization of novel 7-azaindoles and their processing into crystalline AIE structures with stimulated as well as spontaneous emission properties. The optical properties in solution were measured and a large redshift in the emission is observed upon the BF_2 complexion whereas N1-alkyl chain led to unsubstantial PL changes. All crystals exhibit green luminescence with slight PL spectral changes likely attributed to the different molecular packing and optical waveguiding properties. By deploying a combination of X-ray diffraction, steady state, and time resolved PL spectroscopy and DFT as well as TD-DFT calculations, we provide insights into the interrelation and interdependence between structure and luminescence properties. Furthermore, 100 µm long needles displayed optical waveguiding and notable random lasing performance. This is achieved by partially inhibiting structural relaxation which drives non radiative decay, a critical factor for effective lasing, highlighting the potential of these materials for future optoelectronic applications.

4. Experimental Section

General: All chemicals used were purchased from an available commercial source and used without further purification. Nuclear magnetic resonance (^{1}H and ^{13}C) spectra were recorded on a Bruker AVANCE 300 MHz spectrometer. Chemical shifts (δ) are quoted in parts per million (ppm) in reference to the residual peak of $CDCl_3$ (7.26 ppm).

Single-Crystal X-Ray Diffraction: Single Crystal X-Ray Diffraction (SCXRD) of **6** and **8** was performed using a Bruker Kappa Apex II diffractometer using graphite-monochromated molybdenum Kα radiation (λ = 0.71073 Å). The structural models were analyzed with PLATON and the crystal structures were obtained using a MERCURY software. Single Crystal X-Ray Diffraction (SCXRD) of **5** and **7** was performed using XtaLAB Synergy R, HyPix-Arc 100 diffractometer. The crystal was kept at 150.00(10) K during data collection. Using Olex2,[47] the structure was solved with the SHELXT[48] structure solution program using Intrinsic Phasing and refined with the SHELXL[49] refinement package using Least Squares minimization.

The powder of compounds **5** and **6** were enclosed in a vessel under vacuum conditions and heated at 200 °C for some time to gradually vaporize the powder which consequently condensed at the water-cooled walls of the vessel forming the crystals. Crystals from **7** and **8** were produced by slow solvent evaporation in two solvents by dissolving 2 mg of the compound in the minimum amount of CH_2Cl_2 and then pouring 2 mL of petroleum ether in a vial. Crystals from **7** and **8** can slowly grow by evaporation of excess solvents at room temperature.

Optical Spectroscopy Measurements: UV-Steady-State Optical Properties were recorded with a Perkin-Elmer Lambda 950 and a 150 mm integrating sphere. Barium sulfate was used as a 100% reflection reference, while carbon black was used as a 0% reflectance reference. The reflectance was then converted to either Kubelka-Munk or apparent absorbance values for easier interpretation. Steady-state photoluminescence spectra were recorded with a FLS980 (Edinburgh Instruments) photoluminescence spectrometer using a 450 W Xenon arc lamp and a R298P photomultiplier as detector. The absolute photoluminescence quantum yields were determined using the same instrument equipped with an integrating sphere from LabSphere connected through an optical fiber.

Time-Resolved Photoluminescence were accomplished through the time-correlated single photon counting (TCSPC) technique, by using the same FLS980 (Edinburgh Instruments) photoluminescence spectrometer.

Fluorescence microscopy images were acquired with a Nickon Eclipse Ti inverted microscope with dry objectives (100X N.A. 0.8 and 20X N.A. 0.45) coupled to a Shamrock spectrometer (Andor Technology) with a thermoelectrically cooled Newton EM (Andor) CCD. Excitation was provided by a Xenon Lamp (Nikon corp.) model C-SHG1.

Optical waveguide and lasing measurements were conducted with a pulsed Nd:YAG laser (TEEM photonics) at 355 nm and the emission was collected in a free-space configuration by the Princeton Instruments spectrometer (Acton Research) equipped with a liquid nitrogen cooled deep-depleted CCD (Spec-10:400BR, Princeton Instruments). For calculation of optical loss coefficients, the excitation line was scanned along the crystals with the assistance of micrometer control linear stage.

Computational Details: The molecular geometry of the ground state and excited state was performed using the Gaussian 16 (revision A.03) suite of programs.[50] Since this is the first theoretical study of these compounds, we use two global hybrids functionals with different fraction of Hartree-Fock exchange (HF), PBE0 (25% of HF),[51] and M06-2X (54% of HF),[52] and the range-separated CAM-B3LYP functional (HF of 19% (short range) and 65% (long range)[53] in combination with 6–31+G** basis set. The initial geometry for the Density Functional Theory (DFT) calculations and subsequent optimization was extracted from the X-ray structure. The vibrational frequencies were computed to check the nature of the ground state and excited states being all real in all cases. The solvent THF was treated implicitly using the Polarizable Continuum Model (PCM).[54–56] Time-Dependent DFT calculations using TD-PBE0, TD-M06-2X and TD-CAM-B3LYP functionals and 6–31+G** basis set were performed to calculate the vertical electronic transitions. The theoretical emission in solution was calculated as ΔE_{em} = E(S1//S1) – E(S0//S1) where E(S1//S1) is the energy of the S_1 excited state at its equilibrium geometry (using both state-specific solvation approach (SS), and linear response approach (LR))[57] and E(S0//S1) is the energy of the S_0 ground state at the S_1 excited state geometry and with the static solvation from the excited state.[58] The emission in solid-state was computed using a two-layer ONIOM approach[59–61] building a model cluster from the X-ray crystallographic data. The central active molecule was treated with PBE0 (high level) and both S_0 and S_1 electronic state geometries were fully optimized in gas phase. The central molecule was surrounded by 12, 16, 15, and 12 molecules (low level) in compounds **5**, **6**, **7**, and **8**, respectively, treated by molecular mechanics (MM) using the UFF force field[62] to alleviate the computational cost and with their molecular geometries frozen.

The non-radiative vibrational relaxation was estimated by calculating the reorganization energy, λ, using the program DUSHIN[63] according to: $\lambda = \sum_i \lambda_i = \sum_i \hbar\,\omega_i S_i$. ω_i is the wavenumber associated to the vibrational mode i which assists the internal conversion process, and S_i is the dimensionless Huang-Rhys (HR) factor calculated from the atomic displacements (ΔQ), and force constant (k), of the normal mode i according to $S_i = \frac{1}{2}\, k \frac{\Delta Q^2}{\hbar\omega_i}$.

Supporting Information

Supporting Information is available from the Wiley Online Library or from the author.

Acknowledgements

E.M.G.F acknowledges the grant PID2019-105479RB-I00, PID2022-137889OB-I00 and TED2021-131223B-I00 funded by MCIN/AEI/10.13039/501100011033 and by "ERDF A way of making Europe" and A.N. acknowledges by Junta de Andalucía (PAIDI-FQM-337) and Universidad de Jaén, FEDER_UJA_2020 (project 2021/00627/001 and project 2020/1380695). The authors thank the Centro de Servicios de Informática y Redes de Comunicaciones (CSIRC, Universidad de

Granada) for providing the computer time that made this work possible. J.A.C. acknowledges financial support from the European Social fund through "Programa de empleo juvenil y la iniciativa de empleo juvenil" (PEJD-2017-PRE/IND-4536) of the Government of Madrid. J.C.G acknowledges the Spanish Ministry of Science and Innovation (RTI2018-097508–B-I00, PID2021-128313OB-I00, and PDC2023-145871-I00), the Regional Government of Madrid through h projects NMAT2D-CM (S2018/NMT-4511), Proyectos Sinérgicos de I + D (Grant Y2018/NMT-5028 FULMATEN-CM) and NANOCOV-CM (REACT-UE) and a Research Consolidation Grant (CNS2022-136191). C.M. also thanks the MICIU/AEI projects refs. PID2021-128761OA-C22 and CNS2022-136052 funded by MCIN/AEI/10.13039/501100011033 and FEDER, UE. This research was also supported by SBPLY/21/180501/000127, funded by the JCCM and the EU through "Fondo Europeo de Desarollo Regional" (FEDER). IMDEA Nanociencia acknowledges support from the Severo Ochoa Programme for Centres of Excellence in R&D (MINECO, grant CEX2020-001039-S).

Conflict of Interest

The authors declare no conflict of interest.

Data Availability Statement

The data that support the findings of this study are available from the corresponding author upon reasonable request.

Keywords

azaindole, DFT, lasing, organic photonics, TD-DFT

Received: February 16, 2024
Revised: November 7, 2024
Published online: December 23, 2024

[1] Y. Oyama, M. Mamada, A. Shukla, E. G. Moore, S.-C. Lo, E. B. Namdas, C. Adachi, *ACS Mater. Lett.* **2020**, *2*, 161.
[2] H.-H. Fang, J. Yang, J. Feng, T. Yamao, S. Hotta, H.-B. Sun, *Laser Photonics Rev.* **2015**, *9*, 128.
[3] J. Borges-González, C. J. Kousseff, C. B. Nielsen, *J. Mater. Chem. C* **2019**, *7*, 1111.
[4] Z. Hu, J. Wang, X. Ma, J. Gao, C. Xu, K. Yang, Z. Wang, J. Zhang, F. Zhang, *Nano Energy* **2020**, *78*, 105376.
[5] J. Song, H. Lee, E. G. Jeong, K. C. Choi, S. Yoo, *Adv. Mater.* **2020**, *32*, 1907539.
[6] J. Álvarez-Conde, E. M. García-Frutos, J. Cabanillas-Gonzalez, *Molecules* **2021**, *26*, 958.
[7] A. S. D. Sandanayaka, T. Matsushima, F. Bencheikh, S. Terakawa, W. J. Potscavage, C. Qin, T. Fujihara, K. Goushi, J.-C. Ribierre, C. Adachi, *Appl. Phys. Express* **2019**, *12*, 061010.
[8] K. Yoshida, J. Gong, A. L. Kanibolotsky, P. J. Skabara, G. A. Turnbull, I. D. W. Samuel, *Nature* **2023**, *621*, 746.
[9] Q. Zhang, W. Tao, J. Huang, R. Xia, J. Cabanillas-Gonzalez, *Adv. Photonics Res.* **2021**, *2*, 2000155.
[10] A. Khasbaatar, Z. Xu, J.-H. Lee, G. Campillo-Alvarado, C. Hwang, B. N. Onusaitis, Y. Diao, *Chem. Rev.* **2023**, *123*, 8395.
[11] M. Yuan, Y. Qiu, H. Gao, J. Feng, L. Jiang, Y. Wu, *J. Am. Chem. Soc.* **2024**, *146*, 7885.
[12] Z. Peng, N. Stingelin, H. Ade, J. J. Michels, *Nat. Rev. Mater.* **2023**, *8*, 439.
[13] G. v. Bünau, *Berichte Bunsenges. Für Phys. Chem.* **1970**, *74*, 1294.
[14] J. Luo, Z. Xie, J. W. Y. Lam, L. Cheng, H. Chen, C. Qiu, H. Sing Kwok, X. Zhan, Y. Liu, D. Zhu, B. Zhong Tang, *Chem. Commun.* **2001**, *18*, 1740.
[15] X. Li, H. Yang, P. Zheng, D. Lin, Z. Zhang, M. Kang, D. Wang, B. Z. Tang, *J. Mater. Chem. A* **2023**, *11*, 4850.
[16] R. Xu, P. Zhang, Q. Shen, Y. Zhou, Z. Wang, Y. Xu, L. Meng, D. Dang, B. Z. Tang, *Coord. Chem. Rev.* **2023**, *477*, 214944.
[17] P. Meng, A. Lau, D. Miyajima, Z. Zhao, P. Alam, Z. Qiu, B. Z. Tang, *Appl. Phys. Lett.* **2024**, *124*, 100501.
[18] K. Li, Y. Lin, C. Lu, *Chem. – Asian J.* **2019**, *14*, 715.
[19] M. Chen, J. Liu, F. Liu, H. Nie, J. Zeng, G. Lin, A. Qin, M. Tu, Z. He, H. H. Y. Sung, I. D. Williams, J. W. Y. Lam, B. Z. Tang, *Adv. Funct. Mater.* **2019**, *29*, 1903834.
[20] Y. Xiong, J. Gong, J. Liu, D. Wang, H. Wu, Z. Zhao, M. Fang, Z. Li, D. Wang, B. Z. Tang, *J. Mater. Chem. C* **2022**, *10*, 10009.
[21] X. Han, F. Ge, J. Xu, X.-H. Bu, *Aggregate* **2021**, *2*, e28.
[22] Q. Li, Z. Li, *Acc. Chem. Res.* **2020**, *53*, 962.
[23] Q. Liao, Q. Li, Z. Li, *Adv. Mater.* **2023**, 2306617.
[24] X.-M. Cai, Y. Lin, Z. Tang, X. Zhang, T. Mu, S. Huang, Z. Zhao, B. Z. Tang, *Chem. Eng. J.* **2023**, *451*, 138627.
[25] O. Svelto, *Principles of Lasers*, Springer US, Boston, MA, **2010**.
[26] C. Martín, K. Kennes, M. Van der Auweraer, J. Hofkens, G. de Miguel, E. M. García-Frutos, *Adv. Funct. Mater.* **2017**, *27*, 1702176.
[27] J. Álvarez-Conde, A. Garzón-Ruiz, A. Navarro, S. B. Jiménez-Pulido, P. González-Rodríguez, J. Cabanillas-González, E. M. García-Frutos, *J. Mol. Liq.* **2022**, *368*, 120728.
[28] J. Zheng, Y. Li, Y. Cui, J. Jia, Q. Ye, L. Han, J. Gao, *Tetrahedron* **2015**, *71*, 3802.
[29] H. Qian, M. E. Cousins, E. H. Horak, A. Wakefield, M. D. Liptak, I. Aprahamian, *Nat. Chem.* **2017**, *9*, 83.
[30] J. Zheng, F. Huang, Y. Li, T. Xu, H. Xu, J. Jia, Q. Ye, J. Gao, *Dyes Pigments* **2015**, *113*, 502.
[31] L.-Q. Zheng, S. Yang, J. Lan, L. Gyr, G. Goubert, H. Qian, I. Aprahamian, R. Zenobi, *J. Am. Chem. Soc.* **2019**, *141*, 17637.
[32] S. M. Landge, E. Tkatchouk, D. Benítez, D. A. Lanfranchi, M. Elhabiri, W. A. I. Goddard, I. Aprahamian, *J. Am. Chem. Soc.* **2011**, *133*, 9812.
[33] I. Aprahamian, *Chem. Commun.* **2017**, *53*, 6674.
[34] B. Shao, H. Qian, Q. Li, I. Aprahamian, *J. Am. Chem. Soc.* **2019**, *141*, 8364.
[35] R. Arumugam, P. Nayak, B. Dey, R. Kannan, K. Venkatasubbaiah, V. Chandrasekhar, *Dalton Trans.* **2023**, *52*, 7926.
[36] J. Gierschner, J. Shi, B. Milián-Medina, D. Roca-Sanjuán, S. Varghese, S. Park, *Adv. Opt. Mater.* **2021**, *9*, 2002251.
[37] R. Ghosh, F. C. Spano, *Acc. Chem. Res.* **2020**, *53*, 2201.
[38] S. Varghese, S.-J. Yoon, E. M. Calzado, S. Casado, P. G. Boj, M. A. Díaz-García, R. Resel, R. Fischer, B. Milián-Medina, R. Wannemacher, S. Y. Park, J. Gierschner, *Adv. Mater.* **2012**, *24*, 6473.
[39] H. Cao, J. Y. Xu, Y. Ling, A. L. Burin, E. W. Seeling, X. Liu, R. P. H. Chang, *IEEE J. Sel. Top. Quantum Electron.* **2003**, *9*, 111.
[40] S. Varghese, S. K. Park, S. Casado, R. C. Fischer, R. Resel, B. Milián-Medina, R. Wannemacher, S. Y. Park, J. Gierschner, *J. Phys. Chem. Lett.* **2013**, *4*, 1597.
[41] S. Varghese, S. J. Yoon, E. M. Calzado, S. Casado, P. G. Boj, M. A. Díaz-García, R. Resel, R. Fischer, B. Milián-Medina, R. Wannemacher, S. Y. Park, J. Gierschner, *Adv. Mater.* **2012**, *24*, 6473.
[42] S. Varghese, S. K. Park, S. Casado, R. C. Fischer, R. Resel, B. Milián-Medina, R. Wannemacher, S. Y. Park, J. Gierschner, *J. Phys. Chem. Lett.* **2013**, *4*, 1597.
[43] S. J. Yoon, S. Varghese, S. K. Park, R. Wannemacher, J. Gierschner, S. Y. Park, *Adv. Opt. Mater.* **2013**, *1*, 232.
[44] A. Camposeo, M. Polo, P. Del Carro, L. Silvestri, S. Tavazzi, D. Pisignano, *Laser Photonics Rev.* **2014**, *8*, 785.

[45] D. Liu, Q. Liao, Q. Peng, H. Gao, Q. Sun, J. De, C. Gao, Z. Miao, Z. Qin, J. Yang, H. Fu, Z. Shuai, H. Dong, W. Hu, *Angew. Chem., Int. Ed.* **2021**, *60*, 20274.
[46] F. Quochi, F. Cordella, R. Orrù, J. E. Communal, P. Verzeroli, A. Mura, G. Bongiovanni, A. Andreev, H. Sitter, N. S. Sariciftci, *Appl. Phys. Lett.* **2004**, *84*, 4454.
[47] O. V. Dolomanov, L. J. Bourhis, R. J. Gildea, J. a. K. Howard, H. Puschmann, *J. Appl. Crystallogr.* **2009**, *42*, 339.
[48] G. M. Sheldrick, *Acta Crystallogr. Sect. Found. Adv.* **2015**, *71*, 3.
[49] G. M. Sheldrick, *Acta Crystallogr. Sect. C Struct. Chem.* **2015**, *71*, 3.
[50] M. J. Frisch, G. W. Trucks, H. B. Schlegel, G. E. Scuseria, M. A. Robb, J. R. Cheeseman, G. Scalmani, V. Barone, G. A. Petersson, H. Nakatsuji, X. Li, M. Caricato, A. V. Marenich, J. Bloino, B. G. Janesko, R. Gomperts, B. Mennucci, H. P. Hratchian, J. V. Ortiz, A. F. Izmaylov, J. L. Sonnenberg, F. D. Williams, F. Lipparini, F. Egidi, J. Goings, B. Peng, A. Petrone, T. Henderson, D. Ranasinghe, V. G. Zakrzewski et al., *Gaussian 16 Rev. C.01*, Wallingford, CT, **2016**.
[51] C. Adamo, V. Barone, *J. Chem. Phys.* **1999**, *110*, 6158.
[52] Y. Zhao, D. G. Truhlar, *Theor. Chem. Acc.* **2008**, *120*, 215.
[53] T. Yanai, D. P. Tew, N. C. Handy, *Chem. Phys. Lett.* **2004**, *393*, 51.
[54] M. Cossi, N. Rega, G. Scalmani, V. Barone, *J. Comput. Chem.* **2003**, *24*, 669.
[55] J. Tomasi, B. Mennucci, R. Cammi, *Chem. Rev.* **2005**, *105*, 2999.
[56] R. Cammi, S. Corni, B. Mennucci, J. Tomasi, *J. Chem. Phys.* **2005**, *122*, 104513.
[57] R. Improta, V. Barone, G. Scalmani, M. J. Frisch, *J. Chem. Phys.* **2006**, *125*, 054103.
[58] G. Scalmani, M. J. Frisch, B. Mennucci, J. Tomasi, R. Cammi, V. Barone, *J. Chem. Phys.* **2006**, *124*, 094107.
[59] S. Dapprich, I. Komáromi, K. S. Byun, K. Morokuma, M. J. Frisch, *J. Mol. Struct. THEOCHEM* **1999**, *461–462*, 1.
[60] H. Lin, D. G. Truhlar, *Theor. Chem. Acc.* **2007**, *117*, 185.
[61] T. Vreven, K. Morokuma, O. Farkas, H. B. Schlegel, M. J. Frisch, *J. Comput. Chem.* **2003**, *24*, 760.
[62] C. J. Casewit, K. S. Colwell, A. K. Rappe, *J. Am. Chem. Soc.* **1992**, *114*, 10035.
[63] J. R. Reimers, *J. Chem. Phys.* **2001**, *115*, 9103.